

On the Parallel Mechanism of the Dissociation of Energy-Selected $\text{P}(\text{CH}_3)_3^+$ Ions[†]Andras Bodi,[‡] James P. Kercher,[§] Tomas Baer,^{*,§} and Bálint Sztáray[‡]*Department of General and Inorganic Chemistry, Eötvös Loránd University, Budapest, Hungary, and
Department of Chemistry, University of North Carolina, Chapel Hill, North Carolina 27599-3290**Received: August 12, 2004; In Final Form: January 3, 2005*

Energy selected trimethyl phosphine ions were prepared by threshold photoelectron photoion coincidence (TPEPICO) spectroscopy. This ion dissociates via H, CH_3 , and CH_4 loss, the latter two involving hydrogen transfer steps. The ion time-of-flight distribution and the breakdown diagram are analyzed in terms of the statistical RRKM theory, which includes tunneling. Ab initio and DFT calculations provide the vibrational frequencies required for the RRKM modeling. CH_3 loss could produce both the $\text{P}(\text{CH}_3)_2^+$ by a simple bond dissociation step, and the more stable $\text{HP}(\text{CH}_2)\text{CH}_3^+$ ion by a hydrogen transfer step. Quantum chemical calculations are extensively used to uncover the reaction scheme, and they strongly suggest that the latter product is exclusively formed via an isomerization step in the energy range of the experiment. The data analysis, which includes modeling with the trimethyl phosphine thermal energy distribution, provides accurate onset energies for both H ($E_{0\text{K}} = 1024.1 \pm 3.5$ kJ/mol) and CH_3 ($E_{0\text{K}} = 1024.8 \pm 3.5$ kJ/mol) loss reactions. From this analysis, we conclude that the $\Delta_f H_{298\text{K}}^\circ[\text{HP}(\text{CH}_2)(\text{CH}_3)^+] = 783 \pm 8$ kJ/mol and $\Delta_f H_{298\text{K}}^\circ[\text{P}(\text{CH}_2)(\text{CH}_3)_2^+] = 711 \pm 8$ kJ/mol.

Introduction

The industry-wide use of trisubstituted phosphines as transition metal ligands in catalysis makes them an intriguing subject to investigate.^{1,2} Various phosphine ligands are used to solubilize catalysts in water and, thereby, make catalytic reactions more environmentally friendly.³ Also, numerous alkyl and aryl derivatives can be employed to fine-tune the steric and electronic effects the phosphine ligand has on the metal center thereby influencing catalyst activity and life-cycle. Knowledge of the thermochemistry and bond energies of catalysts is an essential ingredient in understanding how they work and requires solid thermochemical information about the ligands, which is, surprisingly, very sparse for phosphines.⁴

Threshold photoelectron-photoion coincidence spectroscopy^{5–12} permits determining the dissociation rate constant for energy selected ions. The rates, which can be measured by modeling the product-ion time-of-flight (TOF) distributions, provide information about the product ion identity and structure, as well as that of the neutral leaving group, which in turn reveal clues about the reaction mechanism. The heat of formation of the precursor molecule, $\text{P}(\text{CH}_3)_3$, was measured in its liquid form by Long and Sackman¹³ to be -126 ± 4 kJ/mol. When this is combined with the measured heat of vaporization of 29 kJ/mol,¹⁴ we obtain the gas phase heat of formation of -97 ± 4 kJ/mol. Interestingly, Pedley and Rylance¹⁵ list the value as -101 ± 5 kJ/mol, even though it is based on the same data. Because the Pedley and Rylance compilation is checked for self-consistency, it may be that they adjusted this value to be more in line with other values. This heat of formation is not listed in any subsequent compilations of Pedley.^{16,17} With this heat of formation, it is possible to extract information about the product ion heats of formation.

This is a first step in the TPEPICO investigation of a series of $\text{PH}_n\text{R}_{3-n}$ and $\text{NH}_n\text{R}_{3-n}$ molecules. Energy selected electron impact mass spectrometry has already shown that the $\text{N}(\text{CH}_3)_3^+$ ion dissociates primarily by H loss.¹⁸ However, little else is known about the ion chemistry of the other species, especially the phosphor analogues.

Experimental Approach

The apparatus has been previously described with the emphasis on eliminating the “hot” electron contribution to the measurement,¹⁹ so only a brief summary is given here, with special attention to the recent upgrade of the ion and electron optics and detection systems of the spectrometer.

The sample enters the ionization region through a hypodermic needle and is ionized by the incident light from an H_2 discharge lamp dispersed by a 1 m vacuum UV monochromator. The entrance and exit slits were set to 100 μm , which yields a resolution of 1 Å (12 meV at a photon energy of 10 eV). The energies were calibrated against the hydrogen Lyman- α resonance at 1215.67 Å.

The electrons are extracted from the midpoint of a 12 mm wide ionization region by a 20 V/cm field. This is followed by a second acceleration region with a terminal electron energy of 74 eV and a 13 cm long field free drift region. The applied voltages are designed to velocity focus threshold electrons onto a 1.4 mm aperture at the end of the electron drift region, where a Channeltron detects them. At the same time, energetic electrons in a ring around the central spot are collected by a multichannel plate detector (MCP) with a hole in the center to accommodate the channeltron and provide a measure of the hot electron signal. Because the velocity focusing optics selects electrons only on the basis of their perpendicular velocity component, it cannot stop hot electrons with zero perpendicular momentum from reaching the central detector. The hot electron contamination had blemished threshold photoelectron experi-

[†] Part of the special issue “George W. Flynn Festschrift”.^{*} To whom correspondence should be addressed.[‡] Eötvös Loránd University.[§] University of North Carolina.

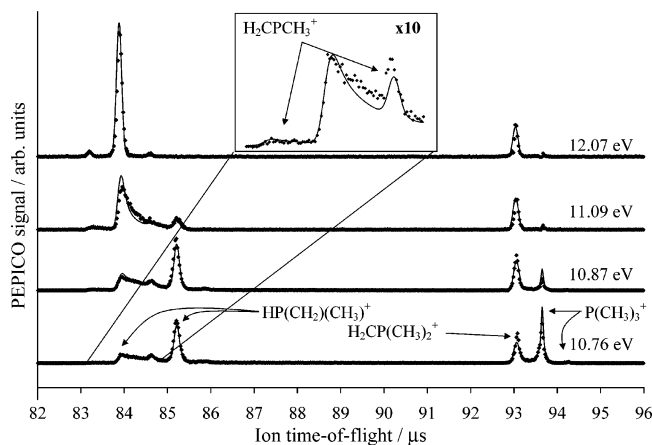


Figure 1. Typical time-of-flight distributions. Dots indicate experiment, whereas solid lines are the fitted diagram from which dissociation limits, rate constants, and entropies of activation are derived.

ments in the past^{20,21} but can now be accounted for by subtracting a fraction of the ring signal from the central signal.^{10,22}

The ions are extracted from the ionization region of 20 V/cm and then accelerated to 104 V. They enter a 40 cm reflectron and are detected using tandem Burle MCPs. Electrons detected in the center and the ring supply start signals, and ions supply the stop signals for two Ortec time-to-pulse-height converters, the outputs of which are fed to Ortec multichannel analyzers to obtain the ion TOF distributions.

The primary experimental information is contained in the ion TOF distribution. In the case of rapid dissociation reactions, the peak shapes are symmetric and only their total areas are of interest. In that case, we can construct a breakdown diagram, which is the plot of relative abundance of the parent and all the daughter ion masses versus the photon energy. Breakdown diagrams without sequential dissociation steps can be modeled in terms of the ion thermal energy distribution, the dissociation onsets for the various parallel dissociation channels, as well as their transition state vibrational frequencies. However, ions with large numbers of internal degrees of freedom and large activation energies dissociate slowly. In this case, dissociation takes place during the course of acceleration, which results in asymmetric TOF distributions from which the dissociation rate constants can be determined. Accounting for these slow reactions is essential for establishing the dissociation energies especially when parallel reaction channels are involved, as is the case for trimethyl phosphine.

Trimethyl phosphine was purchased from Sigma-Aldrich, and was used without further purification. Due to the high volatility of the sample, it could be introduced to the ionization region of the spectrometer through a needle inlet at room temperature.

Experimental Results

TOF mass spectra were acquired in the energy range between 10.53 and 12.73 eV. Typical time-of-flight distributions at selected photon energies are shown in Figure 1. The peak at 93.6 μ s corresponds to the parent ion $\text{P}(\text{CH}_3)_3^+$ (m/z 76). The ^{13}C peak is observable at 94.3 μ s. In this energy range, $\text{P}(\text{CH}_3)_3^+$ loses CH_3 , H, or CH_4 , the corresponding product ions being $\text{HP}(\text{CH}_2)\text{CH}_3^+$ (m/z 61, 83.9 μ s), $\text{P}(\text{CH}_2)(\text{CH}_3)_2^+$ (m/z 75, 93.0 μ s), and $\text{P}(\text{CH}_2)(\text{CH}_3)^+$ (m/z 60, 83.2 μ s), respectively. These three dissociations cannot take place in a sequential manner; thus, all pathways are parallel. As a result, dissociation rate constants must all be of the same order of magnitude to compete

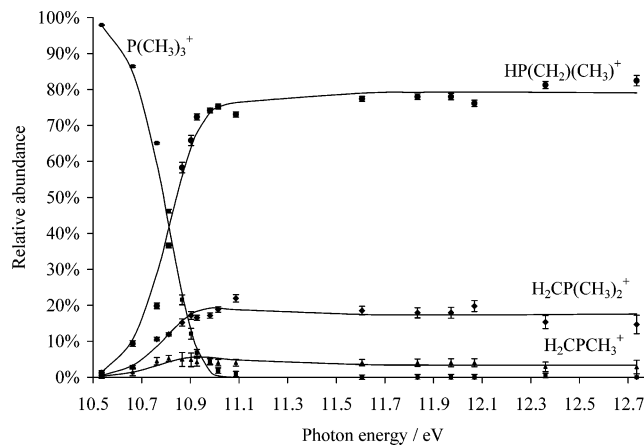


Figure 2. Breakdown diagram. Experimental abundances with their error bars are indicated together with the best fit (solid lines for each species).

with one another. The fractional abundances of the parent and various fragment ions are shown in the breakdown diagram in Figure 2. The relative abundances of the product ions are directly proportional to the ratios of the rate constants of the respective dissociation steps. Since the TOF spectra are asymmetric over a wide energy range, it was also possible to determine the absolute rate constants.

In the lower part of the energy range (<11 eV), all dissociation reactions are slow ($k < 10^7 \text{ s}^{-1}$), so that the ions dissociate during their whole trajectory through the reflectron and to the detector. This explains the asymmetric peak shape observable, e.g., for the methyl loss in the 83.8–85.5 μ s range, which is a result of the methyl loss fragment produced in the acceleration region. The sharp peak at 85.2 μ s is a result of dissociation in the drift region prior to the reflectron. These same two peaks, partly overlapping with the CH_3 -loss peak, but with much less intensity, are also evident for the CH_4 -loss fragment. Ions decaying in the reflecting region contribute to the signal between 85.5 and 93 μ s, which is too weak to be useful for quantitative modeling. Finally, ions decaying in the 2nd field-free drift region, after the reflectron have the same TOF as parent ions. In principle, the H loss peak at 93 μ s is also asymmetric, but the mass resolution renders this feature unobservable. The spectrum at 12.07 eV, when all reactions are fast, shows the three product ions, including the ^{13}C isotope peak for the methyl-loss product at 85.8 μ s. At the three lower energies, we see the effect of dissociation in the first acceleration region and in the drift region before the reflectron.

The probability that the parent ion dissociates in any given time interval is constant with the RRKM framework and is proportional to the sum of the rate constants of the parallel dissociation steps. Thus, the *shape* of the metastable peaks linked to parent ions of the same internal energy are the same. This is born out by the good fit to the data as shown by the solid lines going through the data points. Although the shape of the daughter TOF peaks corresponds only to the sum of the parallel rate constants, the relative peak areas, i.e., product abundances, correspond to their ratios. (Figure 2) Thus, at low energies, the data provide information about the absolute rate constants, while at energies in excess of 11.1 eV, the data in the breakdown diagram provide information only about the ratios of the rate constants.

Modeling

The dissociation of $\text{P}(\text{CH}_3)_3^+$ is modeled in terms of the statistical theory of unimolecular decay, which was developed

TABLE 1: Vibrational Frequencies as Used in the Best Fit

| | |
|---|---|
| PMe_3 B3LYP/6-311G(d), as is | 180, 198, 204, 244, 249, 284, 636, 691, 694, 797, 844, 846, 961, 962, 977, 1319, 1320, 1343, 1457, 1464, 1464, 1472, 1473, 1480, 3012, 3014, 3014, 3090, 3091, 3091, 3104, 3105, 3105 |
| PMe_3^+ B3LYP/6-311G(d), as is | 128, 151, 158, 232, 235, 236, 620, 749, 752, 817, 819, 823, 979, 992, 993, 1328, 1330, 1355, 1415, 1434, 1434, 1437, 1438, 1458, 3017, 3018, 3023, 3106, 3108, 3110, 3139, 3141, 3142 |
| TS to $\text{P}(\text{CH}_2)(\text{CH}_3)_2^+$ B3LYP/6-311G(d), <i>fit</i> , $f = 0.60$ | 35, 53, 112, 130, 173, 234, 275, 609, 636, 756, 810, 847, 932, 958, 971, 972, 1115, 1360, 1372, 1436, 1443, 1460, 1461, 1470, 3052, 3053, 3131, 3132, 3153, 3153, 3158, 3261 |
| TS to $\text{HP}(\text{CH}_2)(\text{CH}_3)^+$ B3LYP/6-311G(d), <i>fit</i> , $f = 1.15$ | 21, 47, 63, 106, 219, 229, 240, 271, 687, 707, 715, 730, 891, 951, 968, 1019, 1101, 1360, 1415, 1417, 1432, 1446, 1462, 2546, 3052, 3097, 3139, 3153, 3155, 3261, 3273, 3275 |
| TS to $\text{P}(\text{CH}_2)(\text{CH}_3)^+$ B3LYP/6-311G(d), <i>fit</i> , $f = 0.63$ | 117, 138, 171, 187, 302, 258, 342, 664, 693, 732, 769, 825, 871, 932, 965, 1179, 1251, 1368, 1395, 1435, 1446, 1463, 1472, 1696, 2982, 3042, 3110, 3117, 3130, 3144, 3204, 3245 |

by Rosenstock et al.²³ as the quasi-equilibrium theory (QET) and by Rice, Ramsperger, Kassel and Marcus,^{24–26} and is known as the RRKM theory. In the present case, tunneling through a hydrogen atom transfer barrier appears to be the important ultimate step in forming the methane-loss product, so we need to incorporate tunneling into the RRKM formalism. This is most easily done by treating the reaction coordinate as a separable coordinate and modeling it with an Eckart barrier.²⁷ Its three variables are the forward and backward activation barriers and the critical vibrational frequency (or barrier curvature). Its major virtue is that tunneling probabilities can be expressed in an analytical form.^{28–31} The RRKM rate constant with tunneling is given by³¹

$$k(E) = \frac{\sigma}{h\rho(E)} \int_{-V_1}^{E-V_0} \kappa(\epsilon_1) \rho^\ddagger(E - V_0 - \epsilon_1) d\epsilon_1$$

where $\rho(E)$ and $\rho^\ddagger(E)$ are the density of states of the molecule and the transition state. The $\kappa(\epsilon_1)$ tunneling probability with translational energy in the reaction coordinate of ϵ_1 is a function of the forward and reverse activation energies (V_0 , V_1) and the critical frequency (ν^\ddagger). ϵ_1 is measured from the top of the barrier, being negative below and positive above, and E is the total ion energy. The inclusion of tunneling is important when accurate thermochemical information is desired because reverse activation barriers prevent determination of dissociation limits.

It might appear that the H and CH_3 loss reactions proceed by simple bond breaking steps, whereas the CH_4 loss reaction must involve a hydrogen transfer step. However, our calculations show that the reaction scheme may be more complicated than that. The methyl loss reaction could produce at least three low-lying production structures, $\text{P}(\text{CH}_3)_2^+$, a cyclic $\text{H}_2\text{P}(\text{CH}_2\text{CH}_2)^+$ ion, or $\text{HP}(\text{CH}_2)(\text{CH}_3)^+$. Quantum chemical calculations indicate that the third ion is the most stable, but the reaction path leading to $\text{HP}(\text{CH}_2)(\text{CH}_3)^+$ involves at least two steps, a hydrogen transfer with a reverse barrier among them.

To calculate rate constants and to evaluate the densities of states, vibrational frequencies of the ion and transition states are required. Because these are not experimentally available, we obtained them from quantum chemical calculations using the Gaussian 03 package.³² The molecular structures of neutral $\text{P}(\text{CH}_3)_3$ and the ionic $\text{P}(\text{CH}_3)_3^+$, an isomeric parent ion $\text{HP}(\text{CH}_2)(\text{CH}_3)_2^+$, and the following product ion structures: $\text{P}(\text{CH}_2)(\text{CH}_3)_2^+$, $\text{P}(\text{CH}_3)_2^+$, $\text{H}_2\text{P}(\text{CH}_2\text{CH}_2)^+$, $\text{HP}(\text{CH}_2)\text{CH}_3^+$, and $\text{P}(\text{CH}_2)(\text{CH}_3)^+$. In addition, the transition states for the reactions $\text{P}(\text{CH}_3)_3^+ \rightleftharpoons \text{HP}(\text{CH}_2)(\text{CH}_3)_2^+$, $\text{P}(\text{CH}_3)_3^+ \rightarrow \text{P}(\text{CH}_2)(\text{CH}_3)^+ + \text{CH}_4$, and $\text{HP}(\text{CH}_2)(\text{CH}_3)_2^+ \rightarrow \text{P}(\text{CH}_2)(\text{CH}_3)^+ + \text{CH}_4$ were fully optimized at the DFT (B3LYP) level of theory with 6-311G(d) basis set. The 6-311+G(d,p) basis set was also employed and

TABLE 2: Ancillary Thermochemical Data (kJ/mol)

| | $\Delta_f H_{0\text{K}}^\circ$ | $\Delta_f H_{298\text{K}}^\circ$ | $H_{298\text{K}}^\circ - H_{0\text{K}}^\circ$ |
|---------------------------|--------------------------------|----------------------------------|---|
| CH_3^\bullet | 150.3 ± 0.4^a | 147.1 ± 0.4^b | 10.5^b |
| H^\bullet | 216.0^c | 218.0^c | 6.2^c |
| P(red, triclinic) | | | 3.6^c |
| C(graphite) | | | 1.1^c |
| $\text{H}_2(\text{g})$ | | | 8.5^c |
| $\text{PH}_3(\text{g})$ | | 5.4^d | |
| $\text{PH}_3^+(\text{g})$ | | 957^d | |
| $\text{CH}_4(\text{g})$ | | -74.5^d | |

^a Determined from $\Delta_f H_{0\text{K}}^\circ[\text{CH}_3^+]$ from Weitzel et al.⁴⁸ and $\text{IE}(\text{CH}_3^\bullet)$ from Blush et al.⁴⁹ ^b Methyl radical frequencies used in the calculation were 537, 1402, 1402, 3102, 3282, and 3282 cm^{-1} . ^c From Wagman et al.⁴⁵ ^d From Lias et al.⁵⁰

yielded nearly identical geometries and vibrational frequencies. The stationary points were confirmed to be minima or transition states by vibrational analysis. We could not locate the exact transition state corresponding to the dissociation $\text{HP}(\text{CH}_2)(\text{CH}_3)_2^+ \rightarrow \text{P}(\text{CH}_2)(\text{CH}_3)^+ + \text{CH}_4$; therefore, all ab initio data relating to this species are approximate.

The G3, CBS-QB3, and CCSD(T) methods, the latter with the cc-pVTZ basis set, were employed to acquire ab initio thermochemical data and to improve on B3LYP/6-311G(d) calculations (Tables 1 and 3).

Dissociations without reverse barriers usually have well-defined reaction paths, so the standard frequency analysis yields one imaginary frequency, and $3N - 5$ real ones for the TS. The latter are used to calculate the transition state sums of states, which are needed to calculate the rate constants. Transition state geometries for the direct bond cleavage dissociations were thus generated by stretching the reaction coordinate to 4 Å and carrying out a constrained optimization of the rest of the internal coordinates. In the case of a reaction with a reverse activation barrier and the possibility of tunneling, a sizable portion of the potential energy surface needs to be explored to find the transition state, which is now a saddle point. This was accomplished using QST2 and QST3^{33,34} methods. The reaction path calculations were carried out at the B3LYP/6-311G(d) level, barrier heights were calculated at the CCSD(T)/cc-pVTZ level at the optimized B3LYP/6-311G(d) geometry, with ZPE corrections from the B3LYP frequency analysis. Transition state frequencies of a species were then optimized by multiplying the lowest 2 or 5 frequencies by a constant factor.

The calculated vibrational frequencies are used to obtain the thermal energy distribution of the neutral, activation entropies, zero-point energies where applicable, and density and number of states for ions and transition states, respectively. Scott and Radom³⁵ showed that the B3LYP/6-31G(d) scaling factor for the low-frequency modes, which are of most importance for

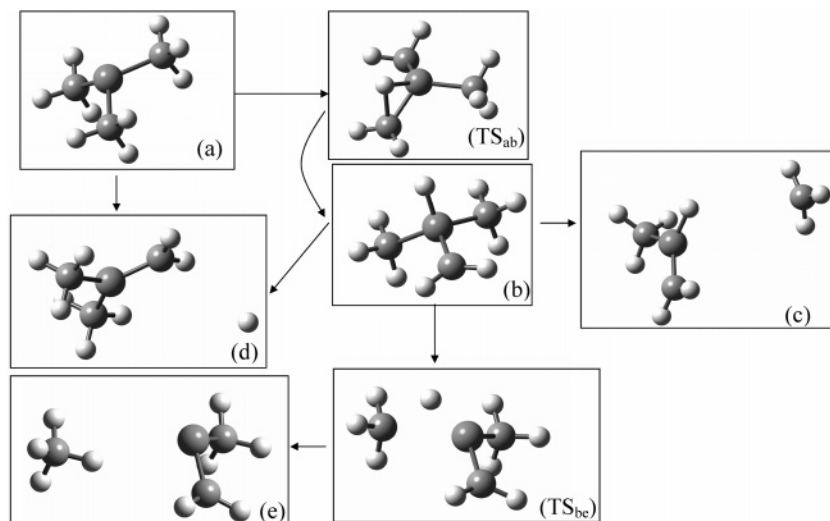


Figure 3. Reaction scheme for H, CH₃, and CH₄ loss from P(CH₃)₃⁺ ions.

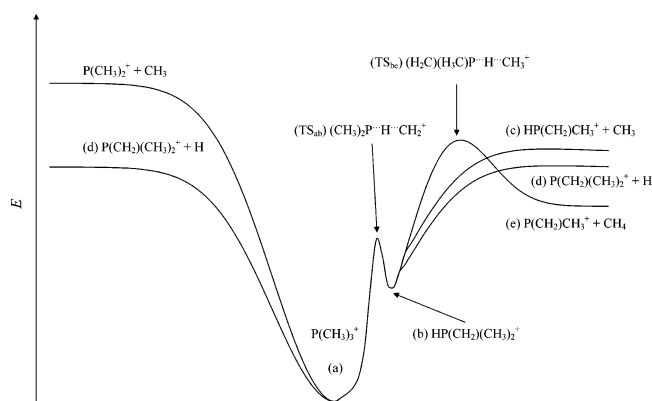


Figure 4. Potential energy diagram with approximate potential energy curves for each reaction. Some pathways discussed in the text are omitted for clarity.

the density of states, is 1.001. We used unscaled B3LYP/6-311G(d) frequencies throughout the calculations, which agreed well with the B3LYP/6-31(d) values (the standard deviation of their ratio was 0.008 for the neutral P(CH₃)₃). High-frequency modes do not affect the density of states very much, therefore they were not scaled, either. Because no phosphorus compounds were included in the Scott and Radom study, it is of course not certain that the same scaling factors hold for P(CH₃)₃. In addition, a comparison between our calculated frequencies and some experimental ones^{36,37} (no complete set of normal modes was derived) showed only modest agreement. We thus varied the assumed frequencies to determine the overall effect on the modeling of the data. The uncertainty in these frequencies translated to an uncertainty of about 1.2 kJ/mol in the derived dissociation limits. To the best of our knowledge, neither experimental data nor published scaling factors are available for the ion frequencies, so we used the calculated ones as starting points for fitting the data. The vibrational frequencies used in the best fit are listed in Table 1.

Discussion

Calculated Reaction Products and Mechanism. The reaction scheme derived from the experimental observations and the ab initio calculations is illustrated in Figures 3 and 4. There are two possible structures for the methyl loss product, P(CH₃)₂⁺ and HP(CH₂)CH₃⁺. The cyclic H₂P(CH₂CH₂)⁺ is kinetically not accessible, nevertheless all were calculated. The G3 and CCSD-

TABLE 3: Results of Quantum Chemical Calculations (kJ/mol)

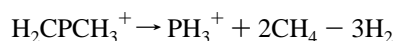
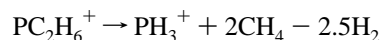
| P(CH ₃) ₃ ⁺ → | ΔE ₀ | |
|---|------------------------------|-----|
| | CCSD(T)/cc-pVTZ ^a | G3 |
| P(CH ₃) ₂ ⁺ + CH ₃ | 304 | 308 |
| TS (CH ₃)P(H ₂ C)⋯H⋯CH ₃ ⁺ | 303 | |
| H ₂ P(CH ₂ CH ₂) ⁺ + CH ₃ | 281 | 286 |
| HP(CH ₂)CH ₃ ⁺ + CH ₃ ^b | 269 | 267 |
| TS (H ₂ C)(H ₃ C)P⋯H⋯CH ₃ ⁺ | ca. 265 | |
| P(CH ₂)(CH ₃) ₂ ⁺ + H ^b | 252 | 248 |
| P(CH ₂)CH ₃ ⁺ + CH ₄ | 239 | 249 |
| TS (CH ₃) ₂ P⋯H⋯CH ₂ ⁺ | 199 | |
| HP(CH ₂)(CH ₃) ₂ ⁺ | 40 | 34 |

^a ZPE calculated using unscaled B3LYP/6-311G(d) frequencies.

^b Experimental value: 242 kJ/mol.

(T) energies showed that the most stable ion is HP(CH₂)CH₃⁺, which involves a hydrogen transfer accompanying the methyl loss step (Table 3). The next most stable ion is a cyclic H₂P(CH₂CH₂)⁺ (19 kJ/mol above HP(CH₂)CH₃⁺), which involves two hydrogen transfers. Finally, the least stable ion, lying 41 kJ/mol above the lowest product ion structure, is P(CH₃)₂⁺, which can be produced by direct loss of CH₃ from the parent ion. The only reasonable structure for the H loss ion is P(CH₂)(CH₃)₂⁺, which can be obtained by direct homolytic bond cleavage from the parent ion and has a predicted onset energy 18 kJ/mol below the lowest energy methyl loss barrier. Finally, the most stable CH₄ loss ion has the H₂CPCH₃⁺ structure, which can only be produced by an accompanying hydrogen-transfer step and has a calculated dissociation limit that is very close to that of the H-loss reaction.

The heats of formation for these species (Table 4) were also obtained by using the G3 and CBS-QB3 298 K enthalpies to calculate the heats of reaction for the following reactions along with previously published heats of formation of the right-hand side compounds (Table 2)



Although the experimentally observed onsets for the three channels are nearly identical, their intensities are not. In fact,

TABLE 4: Calculated and Experimental 298 K Heats of Formation (kJ/mol)

| species ^a | G3 ^b | CBS-QB3 ^b | $(H_{298\text{K}}^\circ - H_{0\text{K}}^\circ)_{\text{G3}}^c$ | expt. |
|--|-----------------|----------------------|---|----------------|
| $\text{P}(\text{CH}_3)_3$ | -108.3 | -113.2 | 20.4 | -101 ± 5^d |
| $\text{P}(\text{CH}_3)_3^+$ | 655.6 | 647.6 | 21.4 | $682^{e,e}$ |
| $\text{P}(\text{CH}_3)_2^+$ | 824.7 | 822.2 | 16.5 | |
| $\text{H}_2\text{P}(\text{CH}_2\text{CH}_2)^+$ | 799.4 | 793.3 | 13.0 | |
| $\text{HP}(\text{CH}_2)(\text{CH}_3)^+$ | 783.0 | 780.5 | 15.9 | 783 ± 8^b |
| $\text{P}(\text{CH}_2)(\text{CH}_3)^+$ | 980.5 | 967.0 | 15.4 | f |
| $\text{P}(\text{CH}_3)_2(\text{CH}_2)^+$ | 687.3 | 683.7 | 20.1 | 711 ± 8^b |

^a Based on ab initio calculations and published experimental heats of formations as described in the text. ^b This work. ^c Calculated using the NIST Webbook 0 K convention of $(H_{298\text{K}}^\circ - H_{0\text{K}}^\circ)_{\text{electron}} = 0$. ^d Reference 15. ^e IP = 8.11 eV.⁴² ^f Experimental heat of formation could not be determined due to the high uncertainty in the CH_4 -loss dissociation limit.

the product ion intensities are nearly the inverse of the calculated onset energies, with the CH_4 loss channel being the least favorite. A second anomaly is the strong CH_3 loss product channel. On the basis of the calculations, it would appear that its structure is $\text{HP}(\text{CH}_2)\text{CH}_3^+$, making its onset energy slightly above that of the H-loss reaction. In addition, this methyl-loss product can only be produced with an accompanying H-atom transfer, whereas the H-loss channel may be direct. The methyl-loss entropy of activation should therefore be considerably less than that of the H-loss channel so that methyl loss should not be a major channel. Finally, our calculations show that the transition state leading to the product ion $\text{HP}(\text{CH}_2)\text{CH}_3^+$ from $\text{P}(\text{CH}_3)_3^+$ has an activation energy well beyond the studied energy range. To resolve these contradictory experimental and quantum chemical results, we searched for a low energy isomerization step that would accommodate both. The calculations showed that the parent ion can isomerize with almost no reverse activation energy by the following reaction:



to produce a four coordinated ion with an energy of 34.4 kJ/mol (G3 value) above the parent ion. It is evident that from this structure, we can generate the lowest energy CH_3 and the H loss products by simple homolytic bond cleavages. On the other hand, the CH_4 loss channel can evolve from neither this isomer nor the original $\text{P}(\text{CH}_3)_3^+$ ion without a hydrogen transfer, which can account for its low intensity. Tunneling through an H atom transfer barrier must therefore also be considered here.

We conclude that the methyl loss takes place according to a two step mechanism beginning with a rapid isomerization, followed by a homolytic bond cleavage step. There is neither experimental nor calculated evidence to distinguish between the two possible hydrogen-loss channels, i.e., direct H loss and H loss through the isomer parent ion, so both may be involved. Two possible mechanisms for CH_4 loss were explored. If the H transfer takes place from the parent $\text{P}(\text{CH}_3)_3^+$, the CH_4 loss reaction is accompanied by a significantly higher reverse barrier (60 kJ/mol) and a tighter transition state than if methane is lost from the isomer parent ion, $\text{HP}(\text{CH}_2)(\text{CH}_3)_2^+$ (structure b in Figures 3 and 4) for which the reverse barrier is ca. 25 kJ/mol. In addition, the transition state is much looser in the latter step. We thus conclude that the methane-loss occurs through the isomer parent ion.

Simulation of Experimental Data. The experimental TOF distributions and the breakdown curves were simulated by taking into account the molecule's thermal energy distribution, the dissociation rate constants as functions of the internal energy,

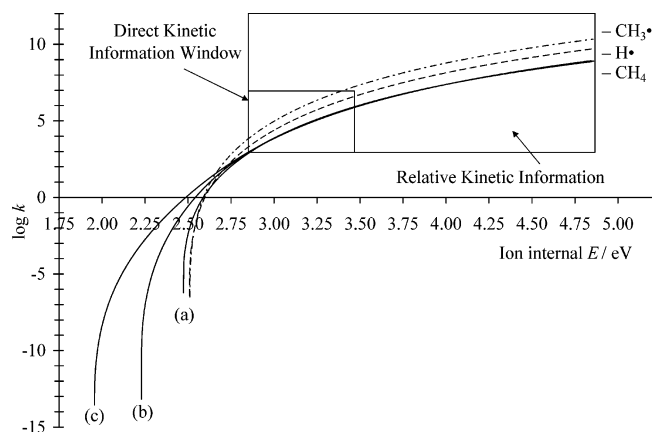


Figure 5. Derived RRKM rate constants for the three dissociation channels. Three CH_4 loss rate constants are shown for various assumed product energies. All three curves coincide in the experimentally sensitive range, although (a) was fitted without tunneling, (b) with a reverse barrier of 2500 cm^{-1} , and (c) with a reverse barrier of 5000 cm^{-1} . Based on quantum chemical calculations, a rate curve closest to (b) is believed to be valid.

the 0 K activation energies, and the reverse barrier of the methane-loss reaction. The thermal distribution of the sample was calculated using the rotational constants and the neutral frequencies. As both can be reliably and relatively accurately estimated by DFT methods, these parameters were kept fixed. Other fixed parameters included the ion acceleration and drift distances, acceleration voltages, ion masses, as well as the neutral and molecular ion vibrational frequencies. Variable parameters were the transition state frequencies (the lowest-lying 2 vibrations for H loss and the lowest 5 for CH_3 and CH_4 losses that turn into barrierless translations and rotations as the products are formed), the dissociation energies, as well as the tunneling parameters V_1 and the critical frequency ν^\ddagger , which were used as input in the RRKM calculation. The fitting of the data was accomplished by use of the downhill simplex method.^{38,39}

For methane loss, both the reverse barrier and the critical frequency were fit. The best fits for the data are shown as solid lines in Figures 1 and 2. The corresponding rate constants as a function of the ion energy are shown in Figure 5.

Figure 5 also highlights the interval in which metastable species can be observed and direct kinetic information can be extracted from the measurement. If a reaction rate constant is $k > 10^7 \text{ s}^{-1}$, the product ion TOF peaks will have symmetric Gaussian shapes so that no direct measure of the rate constant can be obtained. In the slow dissociation limit, rate constants less than 10^3 s^{-1} will yield an insufficient quantity of product ions to be observed. On account of our long ion time-of-flights, the lower limit is quite close to the theoretical one, below which IR fluorescence takes over the dissociation regime.^{40,41}

Since the reaction rate constants in the tunneling regime are extremely slow, we have no direct experimental confirmation about the tunneling step for CH_4 loss. The only experimental parameter associated with this reaction is the location of the barrier, which must be very close to the H and CH_3 loss dissociation limits.

As there are a number of fitting parameters, the stability of the fit and the inherent errors of it are intriguing issues. The error analysis was carried out as follows. To check the flexibility of the fit with regards to dissociation limits, each of the optimized barriers was systematically increased and decreased by a set of energies, and all but one parameter were optimized afterward. Error limits were acquired by checking the fits against

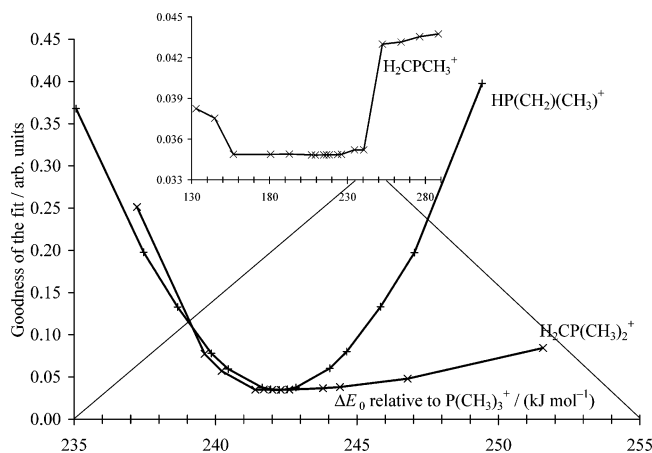


Figure 6. Fit sensitivity to assumed energies.

experimental data. Errors due to uncertainties in the temperature and thermal energy distribution were guessed by changing the experimental temperature or scaling the neutral frequencies, and optimizing all parameters to acquire the best fit.

The goodness of the fit vs the change in the respective barrier is plotted in Figure 6. As can be seen in the diagram, the fit is quite reliable unless tunneling is involved. The response of the fit to changing the H-loss barrier is asymmetrical and somewhat attenuated compared to that of the methyl-loss barrier. This can be attributed to the overwhelming abundance of the methyl-loss product, which means that the same relative error for both reaction channels will affect the goodness of the methyl-loss fit considerably more. However, a wider error range does not necessarily follow, because the H loss breaks down qualitatively (e.g., does not reproduce a constant abundance over a wide energy range) at roughly the same deviation from the optimal barrier. The asymmetrical nature of the curve is also a result of the interplay between the various dissociation products. As the H-loss barrier is decreased causing an increase in the H loss product, the methyl loss product needs to decrease in order to fit the parent ion breakdown curve. The methane loss channel being already very small cannot help out, which causes the methyl loss breakdown curve to be off. On the other hand, when the H-loss barrier is increased, the methyl- and methane-loss channels work hand-in-hand to compensate for the lost H-loss product, thus alleviating the total effect on the goodness of the fit. In brief, a conservative error estimate for both fits is $\pm 150 \text{ cm}^{-1}$, which is $\pm 1.8 \text{ kJ/mol}$. The resolution of the light source adds a further $\pm 0.5 \text{ kJ/mol}$. The previously discussed issue of handling of the low-frequency modes in the neutral and the experimental temperature adds a further $\pm 100 \text{ cm}^{-1}$, i.e., $\pm 1.2 \text{ kJ/mol}$. The fitted barrier heights for the methyl and hydrogen losses, $20\,258 \text{ cm}^{-1}$ (242.3 kJ/mol) and $20\,198 \text{ cm}^{-1}$ (241.6 kJ/mol), correspond to 0 K onsets of 1024.8 ± 3.5 and $1024.1 \pm 3.5 \text{ kJ/mol}$, respectively (IP = 8.11 eV).⁴²

The methane-loss goodness-of-fit diagram (insert in Figure 6) shows a large interval in which tunneling parameters can compensate for the change in the dissociation limit. This greatly impedes our ability to determine an experimental dissociation limit reliably.

The entropies of activation provide a valuable insight into the dissociation kinetics. These are 59.4 and 41.5 J/Kmol (at 600 K) for the methyl- and hydrogen-loss channels, respectively, indicating that these are very loose transition states. On the other hand, the entropy of activation for the tunneling methane loss channel is 25.5 J/Kmol , which is considerably less. It is interesting that this entropy is not negative as is normally

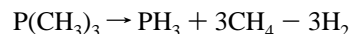
expected for a tight transition state involving tunneling,^{43,44} which suggests that this reaction has a quite loose transition state.

Thermochemical Data. The experimental onsets determined in the previous section can be used to derive experimental heats of formation for the $\text{HP}(\text{CH}_2)(\text{CH}_3)^+$ and $\text{P}(\text{CH}_2)(\text{CH}_3)_2^+$ ions. These are obtained by the following equations:

$$\Delta_f H_{0\text{K}}^\circ[\text{HP}(\text{CH}_2)(\text{CH}_3)^+] = E_0[-\text{CH}_3] + \Delta_f H_{0\text{K}}^\circ[\text{P}(\text{CH}_3)_3] - \Delta_f H_{0\text{K}}^\circ[\text{CH}_3]$$

$$\Delta_f H_{0\text{K}}^\circ[\text{P}(\text{CH}_3)_2\text{CH}_2^+] = E_0[-\text{H}] + \Delta_f H_{0\text{K}}^\circ[\text{P}(\text{CH}_3)_3] - \Delta_f H_{0\text{K}}^\circ[\text{H}]$$

The experimental 298 K heat of formation¹³ of $\text{P}(\text{CH}_3)_3$ is listed in Pedley and Rylance¹⁵ as $-101 \pm 5 \text{ kJ/mol}$, a value confirmed by our G3 and CBS-QB3 calculated heat for the reaction



used in conjunction with the experimental heats of formation for PH_3 , and CH_4 (Table 4).

This value can be transformed to $\Delta_f H_{0\text{K}}^\circ[\text{P}(\text{CH}_3)_3]$ by a thermochemical cycle employing the known $H_{298\text{K}}^\circ - H_{0\text{K}}^\circ$ for the elements as listed by Wagman et al.⁴⁵ and the G3 calculated $H_{298\text{K}}^\circ - H_{0\text{K}}^\circ$ for $\text{P}(\text{CH}_3)_3$ (20.4 kJ/mol) by

$$\Delta_f H_{0\text{K}}^\circ = \Delta_f H_{298\text{K}}^\circ + \sum (H_{298\text{K}}^\circ - H_{0\text{K}}^\circ)_{\text{elements}} - (H_{298\text{K}}^\circ - H_{0\text{K}}^\circ)_{\text{molecule}}$$

which yields $\Delta_f H_{0\text{K}}^\circ[\text{P}(\text{CH}_3)_3] = -76.3 \pm 5 \text{ kJ/mol}$. (For ancillary thermochemical data see Table 2.) Therefore, $\Delta_f H_{0\text{K}}^\circ[\text{HP}(\text{CH}_2)(\text{CH}_3)^+] = 798.2 \pm 8 \text{ kJ/mol}$, and $\Delta_f H_{0\text{K}}^\circ[\text{P}(\text{CH}_3)_2\text{CH}_2^+] = 731.8 \pm 8 \text{ kJ/mol}$. Again G3 $H_{298\text{K}}^\circ - H_{0\text{K}}^\circ$ values (15.9 and 20.1 kJ/mol for $\text{HP}(\text{CH}_2)(\text{CH}_3)^+$ and $\text{P}(\text{CH}_3)_2\text{CH}_2^+$, respectively) can be used to convert 0 K heats of formation to 298 K , employing the previous cycle the other way around. Hence

$$\Delta_f H_{298\text{K}}^\circ[\text{HP}(\text{CH}_2)(\text{CH}_3)^+] = 782.8 \pm 8 \text{ kJ/mol}$$

$$\Delta_f H_{298\text{K}}^\circ[\text{P}(\text{CH}_3)_2\text{CH}_2^+] = 711.0 \pm 8 \text{ kJ/mol}.$$

Because no experimental information is available for the CH_4 loss dissociation limit (only the total barrier is known), we cannot determine an experimental value for the heat of formation for the $\text{P}(\text{CH}_2)\text{CH}_3^+$ ion.

Conclusions

We report the TPEPICO breakdown diagram of trimethyl phosphine, the time-of-flight distribution of the ions formed at photon energies between 10.53 and 12.73 eV , and numerous quantum chemical calculations. The parent ion is found to lose a hydrogen atom, a methyl radical, or a methane molecule in the energy range below 13 eV . Several possible dissociation pathways have been considered, and we conclude that both the methyl radical and the methane molecule are produced from a four coordinated parent ion isomer that is formed in a fast, low-barrier hydrogen-transfer reaction. Hydrogen atoms may be lost from both the parent and the isomerized parent ion.

The dissociation path leading to the methane loss involves a hydrogen transfer in the last step and thus has a reverse barrier. Only the barrier height could be determined from our experiment. Accurate onsets were established for the hydrogen- and

methyl-loss reactions because they involve homolytic bond cleavage as their last step. Using ab initio thermal corrections and previously published thermochemical data for the parent molecule, $\text{P}(\text{CH}_3)_3$, we measured the 298 K heat of formation for the two product ions to be $\Delta_f H_{298\text{K}}^\circ[\text{HP}(\text{CH}_2)(\text{CH}_3)^+] = 783 \pm 8 \text{ kJ/mol}$ and $\Delta_f H_{298\text{K}}^\circ[\text{P}(\text{CH}_2)(\text{CH}_3)_2^+] = 711 \pm 8 \text{ kJ/mol}$.

Quantum chemical calculations have been widely used during the past 10 years to interpret the experimental TPEPICO information and to develop reaction schemes.^{46,47} The results reported here on a relatively small ion use considerably higher level calculations, especially G3, CBS-QB3, and CCSD(T). Their high accuracy ($\approx \pm 10$ – 15 kJ/mol) was sufficient to exclude reaction pathways on which there was no experimental data, and thus they have played an important role in interpreting the experiment.

Acknowledgment. We are grateful to the U.S. Department of Energy for financial support as well as to the International Office of the U.S. National Science Foundation and the Hungarian Academy of Science for a joint U.S. Hungary grant. B.S. gratefully acknowledges the support of the Magyary Zoltán Fellowship granted by the Alapítvány a Magyar Felsőoktatásért és Kutatásért.

References and Notes

- (1) Pinault, N.; Bruce, D. W. *Coord. Chem. Rev.* **2003**, *241*, 1–25.
- (2) Valentine, D. H., Jr.; Hillhouse, J. H. *Synthesis* **2003**, *16*, 2437–2460.
- (3) Vancheesan, S.; Jesudurai, D. *Catalysis* **2002**, *311*–337.
- (4) Lias, S. G.; Bartmess, J. E.; Liebman, J. F.; Holmes, J. L.; Levin, R. D.; Mallard, W. G. *Gas-Phase Ion and Neutral Thermochemistry*, *J. Phys. Chem. Ref. Data*; NSRDS: U.S. Government Printing Office: Washington, DC, 1988; Vol 17, Suppl. 1.
- (5) Dannacher, J.; Rosenstock, H. M.; Buff, R.; Parr, A. C.; Stockbauer, R.; Bombach, R.; Stadelmann, J. P. *Chem. Phys.* **1983**, *75*, 23–35.
- (6) Nishimura, T.; Zha, Q.; Meisels, G. G. *J. Chem. Phys.* **1987**, *87*, 4589–4597.
- (7) Duffy, L. M.; Keister, J. W.; Baer, T. *J. Phys. Chem.* **1995**, *99*, 17862–17871.
- (8) Norwood, K.; Ali, A.; Flesch, G. D.; Ng, C. Y. *J. Am. Chem. Soc.* **1990**, *112*, 7502–7508.
- (9) Thissen, R.; Alcaraz, C.; Hepburn, J. W.; Vervloet, M.; Dutuit, O. *Int. J. Mass Spectrom.* **2000**, *199*, 201–209.
- (10) Li, Y.; Sztáray, B.; Baer, T. *J. Am. Chem. Soc.* **2001**, *123*, 9388–9396.
- (11) Weitzel, K. M.; Mähner, J.; Baumgärtel, H. *Ber. Bunsen-Ges. Phys. Chem.* **1993**, *97*, 134–139.
- (12) Weitzel, K. M.; Mähner, J. *Z. Phys. Chem.* **1996**, *195*, 181–193.
- (13) Long, L. H.; Sackman, J. F. *Trans. Faraday Soc.* **1957**, *53*, 1606–1611.
- (14) Rosenbaum, E. J.; Sandberg, C. R. *J. Am. Chem. Soc.* **1940**, *62*, 1622–1623.
- (15) Pedley, J. B.; Rylance, J. *Sussex-NPL Computer Analysed Thermochemical Data: Organic and Organometallic Compounds*; University of Sussex: Sussex, U.K., 1977.
- (16) Pedley, J. B.; Naylor, R. D.; Kirby, S. P. *Thermochemical Data of Organic Compounds*; Chapman and Hall: London, 1986.
- (17) Pedley, J. B. *Thermochemical Data and Structures of Organic Compounds*; Thermodynamics Research Center: College Station, TX, 1994.
- (18) Lossing, F. P.; Lam, Y. T.; Maccoll, A. *Can. J. Chem.* **1981**, *59*, 2228–2231.
- (19) Sztáray, B.; Baer, T. *Rev. Sci. Instrum.* **2003**, *74*, 3763–3768.
- (20) Das, P. R.; Nishimura, T.; Meisels, G. G. *J. Phys. Chem.* **1985**, *89*, 2808–2812.
- (21) Lafleur, R.; Sztáray, B.; Baer, T. *J. Phys. Chem. A* **2000**, *104*, 1450–1455.
- (22) Sztáray, B.; Baer, T. *J. Am. Chem. Soc.* **2000**, *122*, 9219–9226.
- (23) Rosenstock, H. M.; Wallenstein, M. B.; Wahrhaftig, A. L.; Eyring, H. *Proc. Natl. Acad. Sci.* **1952**, *38*, 667–678.
- (24) Kassel, L. S. *J. Phys. Chem.* **1928**, *32*, 225–242.
- (25) Marcus, R. A.; Rice, O. K. *J. Phys. Colloid Chem.* **1951**, *55*, 894–908.
- (26) Rice, O. K.; Ramsperger, H. C. *J. Am. Chem. Soc.* **1927**, *49*, 1617–1629.
- (27) Eckart, C. *Phys. Rev.* **1930**, *35*, 1303–1309.
- (28) Baer, T.; Hase, W. L. *Unimolecular Reaction Dynamics: Theory and Experiments*; Oxford University Press: New York, 1996.
- (29) Miller, W. H. *J. Am. Chem. Soc.* **1979**, *101*, 6810–6814.
- (30) Miller, W. H. *J. Am. Chem. Soc.* **1983**, *105*, 216–220.
- (31) Miller, W. H. *Chem. Rev.* **1987**, *87*, 19–27.
- (32) Frisch, M. J.; Trucks, G. W.; Schlegel, H. B.; Scuseria, G. E.; Robb, M. A.; Cheeseman, J. R.; Montgomery, J. A., Jr.; Vreven, T.; Kudin, K. N.; Burant, J. C.; Millam, J. M.; Iyengar, S. S.; Tomasi, J.; Barone, V.; Mennucci, B.; Cossi, M.; Scalmani, G.; Rega, N.; Petersson, G. A.; Nakatsuji, H.; Hada, M.; Ehara, M.; Toyota, K.; Fukuda, R.; Hasegawa, J.; Ishida, M.; Nakajima, T.; Honda, Y.; Kitao, O.; Nakai, H.; Klene, M.; Li, X.; Knox, J. E.; Hratchian, H. P.; Cross, J. B.; Adamo, C.; Jaramillo, J.; Gomperts, R.; Stratmann, R. E.; Yazyev, O.; Austin, A. J.; Cammi, R.; Pomelli, C.; Ochterski, J. W.; Ayala, P. Y.; Morokuma, K.; Voth, G. A.; Salvador, P.; Dannenberg, J. J.; Zakrzewski, V. G.; Dapprich, S.; Daniels, A. D.; Strain, M. C.; Farkas, O.; Malick, D. K.; Rabuck, A. D.; Raghavachari, K.; Foresman, J. B.; Ortiz, J. V.; Cui, Q.; Baboul, A. G.; Clifford, S.; Cioslowski, J.; Stefanov, B. B.; Liu, G.; Liashenko, A.; Piskorz, P.; Komaromi, I.; Martin, R. L.; Fox, D. J.; Keith, T.; Al-Laham, M. A.; Peng, C. Y.; Nanayakkara, A.; Challacombe, M.; Gill, P. M. W.; Johnson, B.; Chen, W.; Wong, M. W.; Gonzalez, C.; Pople, J. A. *Gaussian 03*, revision A.1; Gaussian, Inc.: Pittsburgh, PA, 2004.
- (33) Peng, C.; Schlegel, H. B. *Isr. J. Chem.* **1994**, *33*, 449–454.
- (34) Peng, C.; Ayala, P. Y.; Schlegel, H. B.; Frisch, M. J. *J. Comput. Chem.* **1996**, *17*, 49–56.
- (35) Scott, A. P.; Radom, L. *J. Phys. Chem.* **1996**, *100*, 16502–16513.
- (36) Durig, J. R.; Craven, S. M.; Bragin, J. J. *Chem. Phys.* **1970**, *53*, 38–50.
- (37) Park, P. J. D.; Hendra, P. J. *Spectrochim. Acta* **1968**, *24A*, 2081–2087.
- (38) Nelder, J. A.; Mead, R. *Comput. J.* **1965**, *7*, 303–333.
- (39) Press, W. H.; Teukolsky, S. A.; Vetterling, W. T.; Flannery, B. P. *Numerical recipes in C. The art of scientific computing*; Cambridge University Press: Cambridge, 1992; pp 408–412.
- (40) Dunbar, R. C.; Chen, J. H.; So, H. Y.; Asamoto, B. *J. Chem. Phys.* **1987**, *86*, 2081–2086.
- (41) Dunbar, R. C. *Mass Spectrom. Rev.* **1992**, *11*, 309–339.
- (42) Hodges, R. V.; McDonnell, T. J.; Beauchamp, J. L. *J. Am. Chem. Soc.* **1980**, *102*, 1327–1332.
- (43) Booze, J. A.; Weitzel, K. M.; Baer, T. *J. Chem. Phys.* **1991**, *94*, 3649–3656.
- (44) Keister, J. W.; Baer, T.; Thissen, R.; Alcaraz, C.; Dutuit, O.; Audier, H.; Troude, V. *J. Phys. Chem. A* **1998**, *102*, 1090–1097.
- (45) Wagman, D. D.; Evans, W. H. E.; Parker, V. B.; Schum, R. H.; Halow, I.; Mailey, S. M.; Churney, K. L.; Nuttall, R. L. *The NBS Tables of Chemical Thermodynamic Properties*, *J. Phys. Chem. Ref. Data*; NSRDS: U.S. Government Printing Office; Washington, 1982; Vol. 11, Suppl. 2.
- (46) Li, Y.; Baer, T. *Int. J. Mass Spectrom.* **2002**, *218*, 37–48.
- (47) Li, Y.; Baer, T. *Int. J. Mass Spectrom.* **2002**, *218*, 19–37.
- (48) Weitzel, K. M.; Malow, M.; Jarvis, G. K.; Baer, T.; Song, Y.; Ng, C. Y. *J. Chem. Phys.* **1999**, *111*, 8267–8270.
- (49) Blush, J. A.; Chen, P.; Wiedmann, R. T.; White, M. G. *J. Chem. Phys.* **1993**, *98*, 3557–3559.
- (50) Lias, S. G.; Bartmess, J. E.; Liebman, J. F.; Holmes, J. L.; Levin, R. D.; Mallard, W. G. *Ion Energetics Data*; In *NIST Chemistry WebBook*, *NIST Standard Reference Database Number 69*; Mallard, W. G., Linstrom, P. J., Eds. National Institute of Standards and Technology: Gaithersburg, MD, 2000; <http://webbook.nist.gov>.